# NJC

Accepted Manuscript


This is an *Accepted Manuscript*, which has been through the Royal Society of Chemistry peer review process and has been accepted for publication.

*Accepted Manuscripts* are published online shortly after acceptance, before technical editing, formatting and proof reading. Using this free service, authors can make their results available to the community, in citable form, before we publish the edited article. We will replace this *Accepted Manuscript* with the edited and formatted *Advance Article* as soon as it is available.

You can find more information about *Accepted Manuscripts* in the Information for Authors.

Please note that technical editing may introduce minor changes to the text and/or graphics, which may alter content. The journal's standard Terms & Conditions and the Ethical guidelines still apply. In no event shall the Royal Society of Chemistry be held responsible for any errors or omissions in this *Accepted Manuscript* or any consequences arising from the use of any information it contains.

ROYAL SOCIETY OF CHEMISTRY

www.rsc.org/njc

## Colour graphic

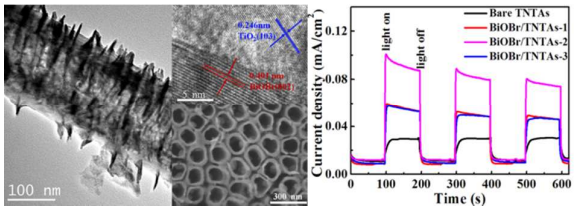


**Text:** New flake-tube structured BiOBr/$TiO_2$ nanotube arrays heterojunction exhibits highly enhanced visible-light photocatalytic activity in pollutant treatment.

Cite this: DOI: 10.1039/c0xx00000x

www.rsc.org/xxxxxx

ARTICLE TYPE

# A Flake-tube Structured BiOBr/$TiO_2$ Nanotube Arrays Heterojunction with Enhanced Visible Light Photocatalytic Activity

**Lili Ruan,[†ab] Jiaqin Liu,[†ab] Qi Zhou,[ab] Jiajia Hu,[ab] Guangqing Xu,[ab] Xia Shu,[ab] Yucheng Wu*[ab]**

***Received (in XXX, XXX) Xth XXXXXXXXX 20XX, Accepted Xth XXXXXXXXX 20XX***

**DOI: 10.1039/b000000x**

In this study, new flake-tube structured BiOBr/$TiO_2$ nanotube arrays (TNTAs) heterojunction has been successfully prepared by anodization followed by sequential chemical bath deposition (S-CBD) method. The as-prepared samples were characterized by X-ray diffraction (XRD), electron microscopy, X-ray photoelectron spectroscopy (XPS) and nitrogen sorption. The photocatalytic activities toward degradation of methyl orange (MO) were evaluated under simulated sunlight. The transient photocurrent response under visible-light irradiation was measured to further confirm the photocatalytic activity enhancement. The results revealed that BiOBr nanoflakes were uniformly dispersed on both inner and outer walls of $TiO_2$ nanotubes, and the BiOBr/TNTAs-2 displayed the best photocatalytic activities, favorable stability and highest photocurrent density among all the BiOBr/TNTAs heterostructured samples. The combined effects of several factors may contribute to the remarkably enhanced photocatalytic activity for the BiOBr/TNTAs-2 sample including open tube-mouth structure, strong visible-light absorption by BiOBr, the formation of BiOBr/TNTAs heterojunction and larger specific surface area.

## 1. Introduction

In recent decades, $TiO_2$ nanotube arrays (TNTAs) has been widely investigated in catalysis due to its superior photocatalytic performance and photoelectric conversion efficiency.[1,2] The highly ordered and hollow tubular structure of TNTAs increases their specific surface area and provides more channels for electron transition.[3-5] Compared with powdered $TiO_2$, TNTAs can immobilize the photocatalyst in the form of film, thus eliminates the particles aggregation and the need for separation or filtration.[6,7] However, with intrinsic wide band gap of 3.2 eV for anatase and 3.0 eV for rutile,[8] $TiO_2$ can only utilize UV light (only 2-3% of the solar spectrum). Moreover, the rapid recombination of photoinduced electrons and holes greatly lowers the quantum efficiency.[9-11] Therefore, it is of great need to develop effective means to broaden light adsorption region and improve the charge separation efficiency of the TNTAs.[12-14] Constructing a heterojunction between TNTAs and other semiconductors with appropriate band gap and band position such as CdS,[15] CdSe,[16,17] $Cu_2O$[18] or ZnO[19] was demonstrated to be an effective way. Under sunlight irradiation, the photo-induced electrons and holes can be easily separated by transferring the electrons or holes to the other semiconductor,[20] assisting the charge separation efficiency and photocatalytic activity enhancement.

As a ternary semiconductor, bismuth oxybromide (BiOBr) with band gap of 2.73 eV has attracted considerable attentions due to its high photocatalytic activity and stability under visible light irradiation.[21-23] BiOBr possesses tetragonal matlockite structure, a layered structure with $[Bi_2O_2]^{2+}$ layers interleaved with double $Br^-$ layers. Both the unique open layered structure and the presence of strong internal static electric field contribute to the effective separation and transfer of the photo-induced electron-hole pairs, assisting high photocatalytic performance of BiOBr.[24-26] Wang's group[27] reported that lamellar structured BiOBr showed high visible-light driven photocatalytic efficiency, which was up to 96% within 120 min. Liu's group[28] described that flowerlike hierarchical BiOBr synthesized by solvothermal Method exhibited excellent photocatalytic activity in degradation of methyl orange (MO) solution under visible-light irradation.

Therefore, constructing a heterojunction between TNTAs and BiOBr can not only broaden the light adsorption range of TNTAs, but also overcome the shortcomings of the powdered BiOBr. However, there is by far no relevant report about BiOBr/TNTAs heterojunction catalyst. In this study, a series of unique flake-tube structured BiOBr/TNTAs heterojunctions were successfully prepared by loading large amounts of BiOBr nanoflakes onto both inner and outer walls of $TiO_2$ nanotubes. Compared with bare TNTAs, the BiOBr/TNTAs heterojunctions showed remarkably enhanced photocatalytic activities under simulated sunlight irradiation, and the BiOBr/TNTAs-2 sample exhibited the best photocatalytic performance as well as the highest photocurrent response. Furthermore, the photocatalytic activity enhancement mechanism of BiOBr/TNTAs heterojunction was also discussed.

## 2. Experimental sections

### 2.1. Materials

$Bi(NO_3)_3.5H_2O$, NaBr, $NH_4F$, acetone, ethylene glycol (EG) and

ethanol were purchased from Sinopharm Chemical Reagent Co.Ltd. All chemicals were of analytical grade and used without further purification. High purity Ti foils (99.7%) were purchased from Beijing Cuibolin Non-ferrous Technology Developing Co.Ltd. Ultrapure water obtained from the Milli-Q system (Millipore, USA) was used to prepare the solutions.

### 2.2. Preparation of self-organized TNTAs

The highly-ordered TNTAs were fabricated via potentiostatic anodization with Ti foil as anode and highly pure graphite foil as cathode. 0.25 M $NH_4F$ ethylene glycol solution containing 8 vol% water was chosen as electrolyte. Before anodization, the Ti foils were degreased in acetone and ethanol with sonication, and then rinsed by ultrapure water and dried at 50 ℃. The anodization process was performed under a constant voltage of 60 V for 2 h. After anodization, the samples were rinsed by sonication in EG for several minutes to remove the debris on the surface, and then washed with ultrapure water to remove the EG. Finally, the as-prepared samples were dried at 50 ℃ and annealed at 500℃ for 2 h with the heating rate of 1℃/min to turn the amorphous TNTAs into the anatase phase.

### 2.3. Preparation of BiOBr/TNTAs samples.

BiOBr/TNTAs samples were prepared via the sequential chemical bath deposition (S-CBD) method. In a typical synthesis process, 1 mmol $Bi(NO_3)_3.5H_2O$ was dissolved in 20 ml 0.1 M mannitol solution to obtain solution A, and 1 mmol NaBr was dissolved in 20 ml ultrapure water to obtain solution B. The above two solutions were placed into the 40℃ water bath. The annealed TNTAs were firstly immersed into solution A for 2 min and rinsed with absolute ethanol, and then immersed into solution B for 2 min and rinsed with absolute ethanol again. The rinsed process was aimed at removing the ions absorbed on the tube-mouth and avoiding mouth blocking by the as-generated BiOBr nanoflakes. Such aforementioned reaction cycle was repeated for 1 to 3 times respectively, and the relevant samples were marked as BiOBr/TNTAs-1, BiOBr/TNTAs-2, BiOBr/TNTAs-3 respectively.

### 2.4. Characterization

Field-emission scanning electron microscope (FESEM) measurements were operated on SU8020 microscope at an accelerating voltage of 5 kV to observe the morphology of the as-prepared samples. The microstructures and the presence of heterojunction of BiOBr/TNTAs were further confirmed using JEM-2100F high-resolution transmission electronic microscopy (HRTEM) operated at 200 kV. The HRTEM samples were prepared by scraping off the TNTAs or BiOBr/TNTAs films and dispersing the scraped powder in ethanol with ultrasonic for 2-3 min, and then placing a drop of the dispersion liquid onto a holey copper grid followed by natural drying. The phase structure was examined by X-ray diffraction (XRD) analysis on Rigaku D/MAX2500V diffractometer with Cu-Kα radiation （λ = 1.5406 Å ） at a scan rate (2θ) of 2° $min^{-1}$. X-ray photoelectron spectroscopy (XPS) measurements were performed on a Thermo ESCALAB 250 XPS system. Nitrogen adsorption isotherms were conducted at 77.15K on SA3100 micromeritics analyzer (Beckman Coulter) after degassing the samples at 373.15K for 2 h. The Brunauer-Emmett-Teller (BET) surface area was estimated by the nitrogen adsorption isotherms in a relative pressure range from 0.05 to 0.2.

### 2.5. Photocurrent and photocatalytic activity test

The transient photocurrent of the as-prepared samples was measured on CHI660D electrochemical workstation in a self-made quartz cell (25W×25L×H30 $mm^3$) with a three-electrode system as illustrated in Fig.1, in which the as-prepared samples served as working electrode, a Pt wire as courter electrode (CE) and Ag/AgCl (3 M KCl) electrode as reference electrode (RE). 0.05 M phosphoric buffer solution (PBS) was employed as electrolyte. A 300 W xenon lamp (HSX-F300, NBET Company) with a 400 nm UV-cut filter positioned 40 cm away was served as visible light source. The transient photocurrent was recorded based on the response to the intermittent visible-light irradiation every 100s at 0.2 V bias with magnetic stirring.

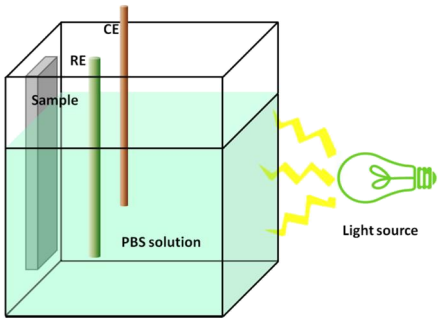


**Fig.1** Schematic illustration of three-electrode system

The photocatalytic activity of the as-prepared samples was evaluated based on the degradation of MO solution (10 mg/L) at ambient temperature. MO is a typical chemically stable nitrogen-containing dye pollutant. 300 W Xenon light was employed as simulated sunlight source positioned 10 cm away from the MO solution. The photocatalytic experiments were carried out on quart tubes surrounded by circulating water. Before illumination, the BiOBr/TNTAs samples in size of 2×2.5 $cm^2$ were submerged into 15 ml MO aqueous solution in the dark for 1 h to achieve the adsorption/desorption equilibrium. Upon illumination, the MO solution was sampled every 30 min to determine the concentration variations on UV-Vis spectrophotometer (Shimadzu UV3600) by recording the variations of the absorption peaks at $\lambda$= 464 nm. The degradation rate (%) can be calculated by the following equation:[29]

$$R = [(C_0 - C)/C_0] \times 100\% = (A_0 - A)/A_0 \quad (1)$$

Herein $R$ is the removal rate, $C_0$ and C are the initial and real-time concentration of MO solution during the reaction; $A_0$ and $A$ are the initial and real-time absorbance values at 464 nm.

## 3. Results and dissicussion

### 3.1. Characterization

The morphologies of the as-prepared samples were firstly observed by FESEM, as illustrated in Fig.2. It is clear that bare TNTAs (Fig.2a) are composed of vertically oriented and highly-ordered nanotubes with an average inner diameter of about 150 nm and wall thickness of 20-30 nm. In addition, the $TiO_2$

nanotubes are well-separated from each other with certain intertube spacings between individual nanotubes. The nanotube surfaces are almost smooth and the tube mouths are open and clean. All microstructures observed above are beneficial for the subsequent deposition reaction. For the sample BiOBr/TNTAs-1 (Fig.2b), it is obvious that both inner and outer walls of the nanotubes are coated by a lot of tiny nanoflakes with only several nanometers in thickness and bout 20-30 nm in width.

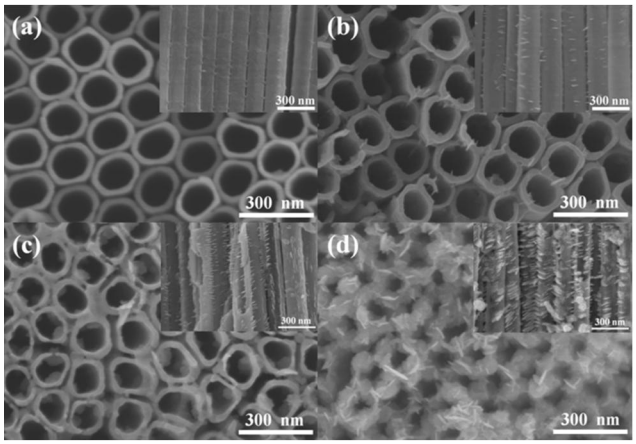


**Fig.2** The FESEM images of (a) bare TNTAs, (b) BiOBr/TNTAs-1, (c) BiOBr/TNTAs-2, (d) BiOBr/TNTAs-3.

For the BiOBr/TNTAs-2 sample with 2 deposition cycles (Fig.2c), more and larger nanoflakes are loaded onto both inner and outer walls of the nanotubes. The nanotubes maintain the hollow structure without mouth blocking, and the intertube spacings remain interconnected. These nanoflakes grow almost perpendicular to the nanotube walls, and this is beneficial for increasing the specific surface area and the effective contact area between the catalyst and the dye solution to be degraded. However, intertube spacings are blocked by the as-generated large nanoflakes (Fig.2d), and the inner diameter of the nanotubes decreases dramatically when the bare TNTAs were deposited via the S-CBD method for 3 cycles, which may not benefit to the solution immersion and weaken its photocatalytic activity. In addition, the complete side view (Fig.3a) and bottom nanotube (marked in Fig.3a) images (Fig.3b) of the BiOBr/TNTAs-2 were further observed. It can be seen clearly that the BiOBr/TNTAs film length is about 25 um, and there are still a lot of nanoflakes loaded on the surface of the bottom nanotubes, further proving the uniform distribution of BiOBr nanoflakes on the whole nanotubes.

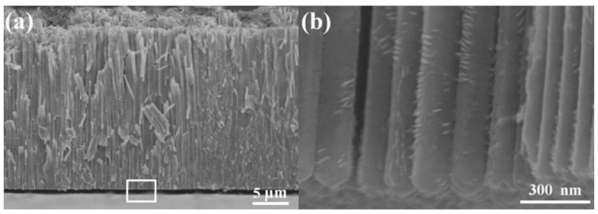


**Fig.3** The complete side view (a) and the bottom nanotube (b) images of the BiOBr/TNTAs-2 sample.

Possible formation mechanism of BiOBr/TNTAs samples have been proposed, as shown in Fig.4. $Bi(NO_3)_3.5H_2O$ was firstly dissolved in mannitol solution and formed Bi-containing complex.[30] When the TNTAs were immersed in solution A, the solution penetrated into the nanotubes and the intertube spacings, and thus the Bi-containing complex was adsorbed to the nanotube walls. When TNTAs was immersed into solution B, large quantity of $Br^-$ would be absorbed to the nanotube walls to react with Bi-containing complex to generate BiOBr nuclei. As the BiOBr tends to crystalline into flake structure,[31] the resulting flake-tube structured heterojunction of BiOBr/TNTAs was formed.

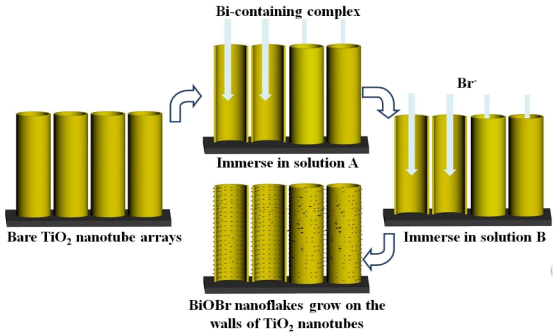


**Fig.4** Schematic illustration of possible formation mechanism of BiOBr/TNTAs heterojunction

The microstructures and the presence of heterojunction for BiOBr/TNTAs-2 sample were further analyzed using TEM and HRTEM, as illustrated in Fig.5. The TEM image (Fig.5a) showed that the BiOBr nanoflakes with a width of 30-50 nm and thickness of several nanometers distribute uniformly over the whole tube walls. It is clear that the nanoflakes are generally perpendicular to the nanotube walls and distribute uniformly over the whole nanotube walls. The corresponding HRTEM image analysis (Fig.5b) indicates that the dark part with a lattice spacing of 4.01 Å corresponds to (002) plane of BiOBr, while the light part with a lattice spacing of 2.46 Å corresponds to (103) plane of $TiO_2$, demonstrating the formation of a heterojunction between BiOBr and $TiO_2$. The TEM and HRTEM results both confirm the FESEM results and the formation of the BiOBr/TNTAs heterojunction.

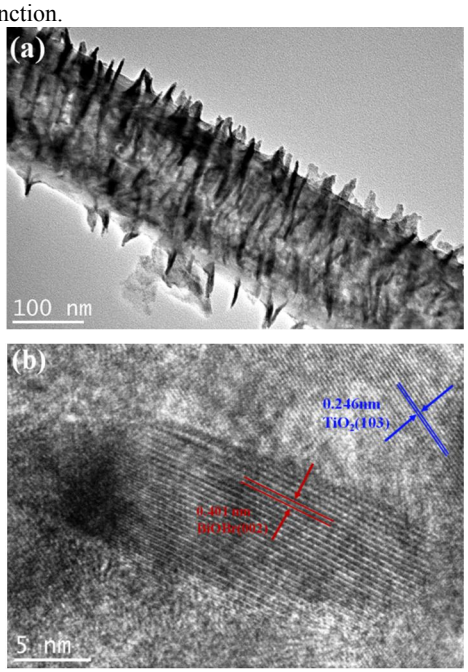


**Fig.5** TEM images (a) and HRTEM images (b) of BiOBr/TNTAs-2

XRD analysis was employed to investigate the phase structure of the as-synthesized samples. Fig.6 shows the XRD patterns of the bare TNTAs and BiOBr/TNTAs samples with different deposition cycles. All the diffraction peaks in pattern (a) can be indexed to anatase $TiO_2$ phase (PDF: 21-1272) except two peaks at around 40.17° and 53.00° which are indexed to (101) and (102) planes of Ti substrate. In the BiOBr/TNTAs patterns, diffraction peaks at 10.9°, 32.22° and 46.20°which can be ascribed to (001), (110) and (200) planes of tetragonal BiOBr appear. In addition, diffraction peaks of BiOBr strengthen gradually with the increase of the deposition cycles, which indicates the increase of BiOBr content in the resulting BiOBr/TNTAs samples. No other impurity peaks can be observed, suggesting that no other Bi-containing impurities exist in the resulting BiOBr/TNTAs samples. All the patterns of BiOBr/TNTAs samples reveal the coexistence of both BiOBr and $TiO_2$ phases, which is consistent with the aforementioned microscopy results.

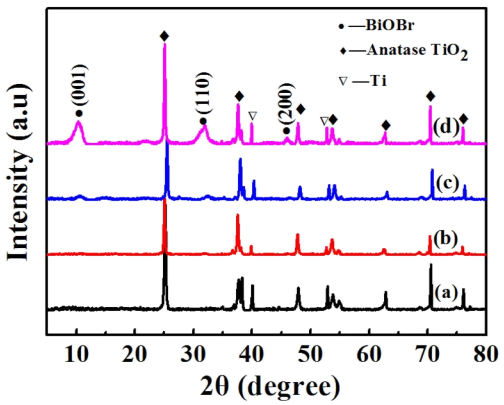


**Fig.6** XRD patterns of (a) TNTAs, (b) BiOBr/TNTAs-1, (c) BiOBr/TNTAs-2, (d) BiOBr/TNTAs-3

To further study the surface composition and chemical state of the BiOBr/TNTAs-2 sample, XPS analysis was conducted, as illustrated in Fig. 7. The survey spectrum (Fig.7a) shows that the BiOBr/TNTAs-2 sample contains not only Ti and O, but also Bi, Br and C elements. The C element detected in XPS spectra may come from $CO_2$ absorbed in the surface of the samples from the air when the samples were exposed in the air. From the high resolution spectrum, two peaks at around 68.04 eV and 69.00 eV are attributed to Br $3d_{5/2}$ and Br $3d_{3/2}$(Fig.7b), which can be ascribed to $Br^-$ in BiOBr.[32] Two peaks at around 159.04 eV and 164.36 eV are assigned to Bi $4f_{7/2}$ and Bi $4f_{5/2}$(Fig.7c), which is characteristic peaks of $Bi^{3+}$ in BiOBr and consistent with the reported values.[33,34] As for Fig.7d, two distinct peaks at around 458.30 eV and 465.80 eV can be observed. The peak at 458.30 eV can be attributed to Ti $2p_{1/2}$,[35] and the peak of 465.80 eV is the stacking of two peaks at 464.44 eV and 466.28 eV respectively. The peak at 464.44 eV corresponds to Ti $2p_{3/2}$,[35] while the peak at 466.28 eV corresponds to Bi 4d.[36] The peaks of Ti 2p are consistent with that of $TiO_2$. Two distinct peaks of O 1s (Fig.7e) at 529.80 eV and 531.4 eV correspond to Ti-O bonds in $TiO_2$[35] and Bi-O bonds in $[Bi_2O_2]^{2+}$ slabs.[33] The XPS results further confirm the coexistence of $TiO_2$ and BiOBr in BiOBr/TNTAs heterojunction and no existence of Bi and Br related impurities, which is in agreement with XRD results.

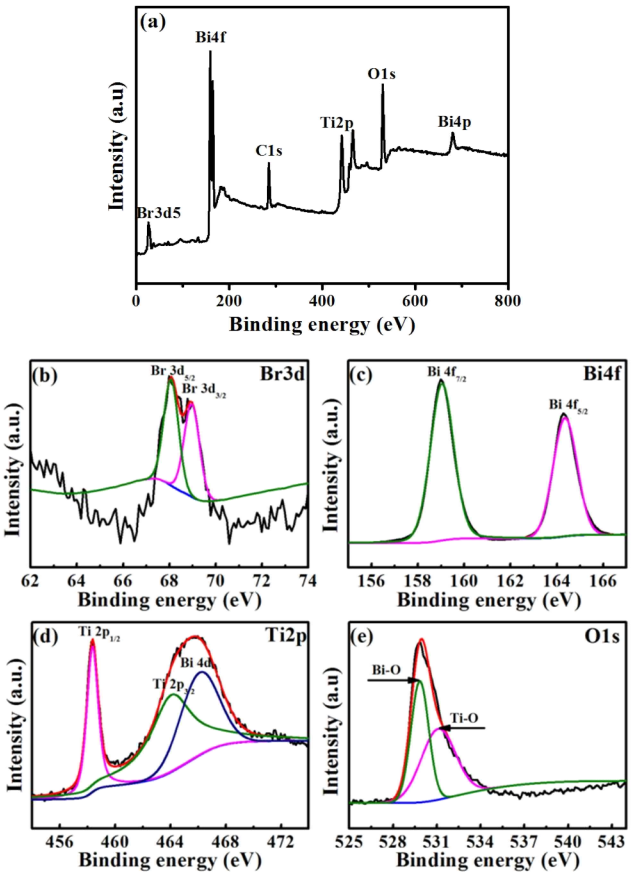


**Fig.7** XPS spectra of BiOBr/TNTAs-2: (a) survey spectrum, (b) Br 3d, (c) Bi 4f, (d) Ti 2p, (e) O 1s

Considering the TNTAs and BiOI/TNTAs films were attached firmly to the Ti substrate and hard to peel off, the relative BET surface area of the resulting samples was measured and calculated via the special self-designed method. Firstly, the redundant part of Ti foil without anodic oxidation was cut off from the resulting samples. Then the obtained rectangular samples were cut into fine shreds and rolled up, subsequently putted into the test quartz tube to measure the Nitrogen adsorption isotherms. If ignore the density differences between the Ti substrate and surface films, the relative BET surface area of the bare TNTAs and BiOBr/TNTAs samples can be calculated via multiplying the measured data by the sample weights and then divided by the sample area, as shown in Table 1.

**Table 1** The relative BET surface area of Ti foils, bare TNTAs and BiOBr/TNTAs samples attached to the Ti substrate.

| samples | Relative BET specific surface area ( $m^2/cm^2$ ) |
|---|---|
| **Ti foil** | $2.5310\times10^{-4}$ |
| **Bare TNTAs** | 0.2732 |
| **BiOBr/TNTAs-1** | 0.3188 |
| **BiOBr/TNTAs-2** | 0.4425 |
| **BiOBr/TNTAs-3** | 0.3096 |

The results show that all the BiOBr/TNTAs samples have higher relative BET surface area than that of bare TNTAs, and BiOBr/TNTAs-2 has the highest surface area. It can be inferred that appropriate amounts of tiny BiOBr nanofakes loaded on the

nanotube surface may increase the specific surface area of the bare TNTAs, while overloading of nanoflakes which stack with each other may lead to the decrease in the specific surface area. Therefore, we deduce that BiOBr/TNTAs-2 sample with the highest relative BET specific surface area may exhibit the highest photocatalytic activity among the BiOBr/TNTAs samples due to its capacity to increase the contact area between adsorbed dye molecules and the catalyst, and improve the molecule transport of reactants and products.

### 3.2 Photocatalytic activity

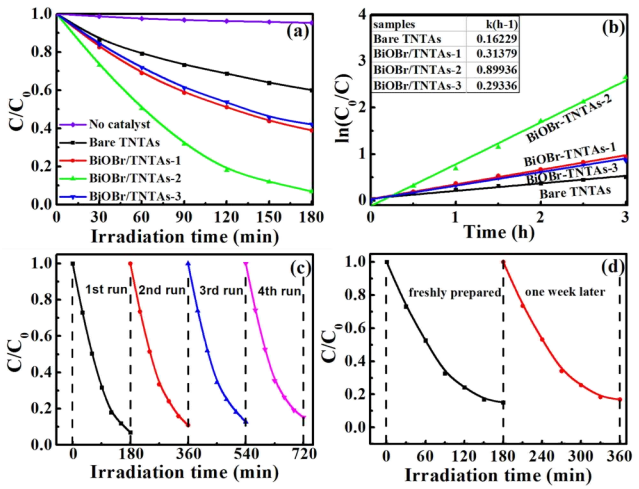


**Fig.8** Photocatalytic performance (a) and the degradation rate constant *k* (b) of bare TNTAs and BiOBr/TNTAs samples under simulated sunlight. Cycling degradation curve of BiOBr/TNTAs-2 for 4 runs(c) and one week later (d)

The photocatalytic performance of the samples was evaluated by the degradation of MO solution under Xenon light irradiation, as shown in Fig.8. It was obvious that MO concentration kept constant with no catalyst added and decreased remarkably with catalyst added. What's more, the BiOBr/TNTAs samples show remarkably enhanced photocatalytic activities than that of bare TNTAs. After 180 min of the photocatalytic reaction, the removal of MO over BiOBr/TNTAs-2 sample reaches 93%, while the degradation rates of MO over BiOBr/TNTAs-1 and BiOBr/TNTAs-3 sample are only 61% and 58% respectively. The results show that loading appropriate amount of BiOBr nanoflakes could effectively enhance the photocatalytic activity of bare TNTAs film under simulated sunlight irradiation. Overloading of BiOBr nanoflakes may lead to the the tube-mouths blocking and intertube spacings disappearance, thus decreasing the BET surface area of the samples and weakening the photocatalytic activity of the BiOBr/TNTAs sample. The process of MO degradation with photocatalysts follows pseudo-first-order model, and the constant *k* can be calculated by the equation:[37]

$$\ln (C_0 / C) = kt \quad (2)$$

Where $C_0$ and $C$ are concentrations of MO solution during the photocatalytic reaction at time 0 and $t$, respectively, and $k$ is the pseudo-first-order rate constant. The $k$ values calculated from the data given in Fig.8a are summarized in Fig.8b. It is clear that BiOBr/TNTAs samples have higher $k$ values than bare TNTAs, and the BiOBr/TNTAs-2 has the highest $k$ value, indicating that BiOBr/TNTAs-2 is the most effective photocatalyst among the resulting BiOBr/TNTAs samples. In addition, the reusability and long-term stability of BiOBr/TNTAs-2 were further evaluated by the cycling tests for 4 cycles (Fig.8c) and one week later (Fig.8d). It can be seen that the photocatalytic efficiency remains stable after 4 cycles and one week later.

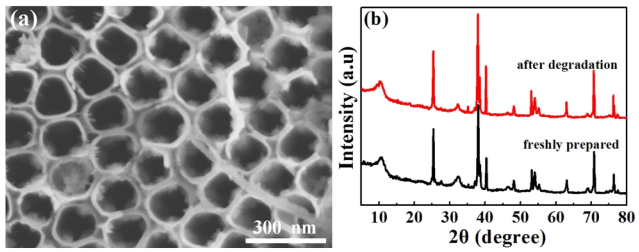


**Fig.9** The SEM image (a) and XRD pattern (b) of BiOBr/TNTAs-2 after photocatalytic degradation.

What's more, no marked changes in the morphology (Fig.9a) and phase structure (Fig.9b) are observed, further proving the high reusability and stability of the BiOBr/TNTAs-2 sample. According to the above analysis, it can be concluded that the BiOBr/TNTAs samples exhibit highly enhanced photocatalytic activity than the bare TNTAs, and the BiOBr/TNTAs-2 sample shows the highest photocatalytic activities as well as great reusability and stability among the BiOBr/TNTAs samples.

### 3.3 The possible mechanism of the photocatalytic activity enhancement in the junction of BiOBr/TNTAs

The possible mechanism of the photocatalytic activity enhancement was also proposed. The schematic diagram for the energy band and possible charge separation mechanism of BiOBr/$TiO_2$ heterojunction was illustrated in Fig.10. BiOBr with the band gap of 2.73 eV can well respond to the visible light,[38] while anatase $TiO_2$ can only be excited by ultraviolet-light due to its intrinsic wide band gap of 3.20 eV. Furthermore, the valence band (VB) of BiOBr (0.31 eV) is lower than that of $TiO_2$ (-0.29 eV), while the conduct band (CB) of BiOBr (3.04 eV) is higher than that of $TiO_2$ (2.91 eV).[38-40] Under Xenon light irradiation, both $TiO_2$ and BiOBr can be excited to generate electron-hole pairs. When BiOBr is contact with $TiO_2$, the energy levels difference between $TiO_2$ and BiOBr can cause the excited electrons flow from the conduction band of $TiO_2$ to that of BiOBr,[41] and captured by $O_2$ adsorbed on the surface of BiOBr/TNTAs catalyst to produce$\cdot O_2^-$. Then $O_2^-$ with strong oxidability can decompose MO to small inorganic molecules. On the contrary, the photo-excited holes on the VB of BiOBr can transfer to that of $TiO_2$, and react directly with MO molecules.[40] Such carriers transfer is known as the Fermi level alignment if the material can be described by Fermi-Dirac distribution.[42] As a result, the photo-induced electron-hole pairs could be effectively separated by the junction formed in the BiOBr/$TiO_2$ interface and the recombination of electron-hole pairs could be reduced, assisting remarkable photocatalytic activity enhancement under simulated sunlight irradiation.

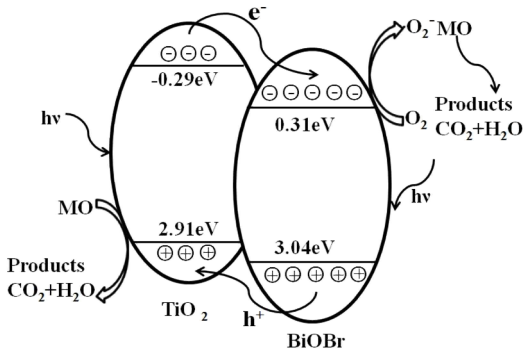


**Fig.10** The schematic diagram for the energy band and possible charge separation mechanism of $BiOBr/TiO_2$ heterojunction

### 3.4 Photocurrent evaluation

Transient photocurrent response can also indicate the photocatalytic activity of the electrode. The transient photocurrent responses of bare TNTAs and BiOBr/TNTAs samples were measured under intermittent visible-light irradiation (300 W Xe light with a 400 nm UV-cut filter), as shown in Fig.11. It is not hard to find that the photocurrent response is prompt and repeatable in the on-off process. Compared with bare TNTAs electrode, the photocurrent intensity of the BiOBr/TNTAs samples significantly enhanced, and the BiOBr/TNTAs-2 sample exhibited the highest photocurrent density.

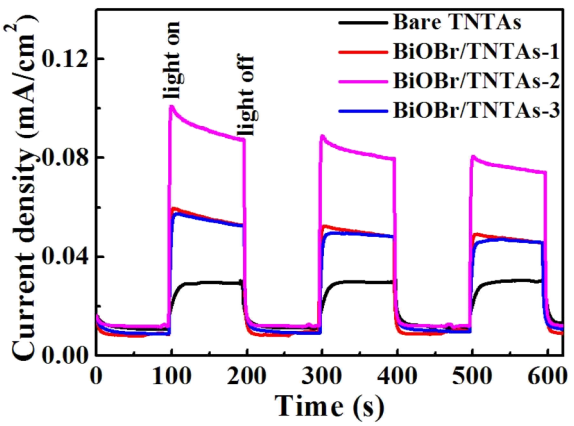


**Fig.11** Comparison of transient photocurrent response of bare TNTAs and BiOBr/TNTAs samples under visible light irradiation at 0.2 V vs. Ag/AgCl.

According to the above analysis and discussion, the reasons for the remarkably enhanced photocurrent intensities of the BiOI/TNTAs-2 sample are mainly due to the combined effects: strong absorption of visible-light by the loaded BiOBr nanoflakes, lower recombination rate of photo-induced electrons and holes by the heterojunction formed in the $BiOBr/TiO_2$ interface, open tube-mouth structure and interconnected intertube spacings after 2 depostion cycles for the facile light injection and solution immersion, and larger specific surface area for increasing the effective contact between the electrode and electrolyte. Moreover, an applied electrostatic field can further enhance the transfer and separation of photo-induced electrons and holes in the BiOBr/TNTAs samples. As for BiOBr/TNTAs-3 sample, the blocking of tube-mouth and intertube spacings by more and larger BiOBr nanoflakes may hinder the injection of light, thus impeding the absorption of BiOBr to visible-light, and thus reducing the generation of photoinduced electron-hole pairs. The photocurrent responses under visible light further demonstrate that the formation of BiOBr/TNTAs heterojunction can broaden the light response range and enhance the photocatalytic activity dramatically, which is in consistence with aforementioned results.

## Conclusions

In this paper, highly-ordered and well-separated TNTAs was firstly prepared by anodization. Then a series of flake-tube structured BiOBr/TNTAs samples were successfully fabricated by loading BiOBr nanoflakes on both inner and outer walls of TNTAs via S-CBD method. The amount and size of BiOBr nanoflakes can be controlled by adjusting the deposition cycles. Compared with bare TNTAs, BiOBr/TNTAs samples exhibit remarkably enhanced photocatalytic activity toward degrading MO under simulated sunlight irradiation, and the BiOBr/TNTAs-2 sample displays the highest photocatalytic activity. Furthermore, the BiOBr/TNTAs-2 sample also exhibits the best photocurrent response among all the BiOBr/TNTAs samples under visible light irradiation. According to comprehensive analysis, it can be concluded that the outstanding photocatalytic activity of BiOBr/TNTAs-2 is due to the combined effects of several factors, including strong visible-light absorption of the loaded BiOBr nanoflaks, the formation of BiOBr/TNTAs heterojunction which contribute to the effective separation and lower recombination of photo-excited electrons and holes, open tube-mouth structure and interconnected intertube spacings for the facile light injection and solution immersion, larger specific surface area resulted from loading tiny BiOBr nanoflakes for increasing the effective contact between dye molecules and catalyst.

## Acknowledgements

We gratefully acknowledge the financial support from the National Natural Science Foundation of China (Nos. 51272062, 51172059, 51202052 and 51102071) and Natural Science Foundation of Anhui province (1408085QE85).

## Notes and references

[a] *Laboratory of Functional Nanomaterials and Devices, Hefei University of Technology, Hefei 230009, China*
[b] *School of Materials Science and Engineering, Hefei University of Technology, Hefei 230009, China. E-mail: ycwu@hfut.edu.c; Fax:+ 86-551-62904517; Tel: + 86-551-62901012*
*† These authors contributed equally to this work.*

1 S. Rani, S.C. Roy, M. Paulose, O.K. Varghese, G.K. Mor, S. Kim, S. Yoriya, T.J. LaTempa and C.A. Grimes, *Phys. Chem. Chem. Phys.*, 2010, , 2780-2800.
2 Z.Y. Liu, Q.Q. Zhang, T.Y. Zhao, J. Zhai and L. Jiang, *J. Mater. Chem.*, 2011, **21**, 10354-10358.
3 Z.X. Sue and W.D. Zhou, *J. Mater. Chem.*, 2011, **21**, 8955-8970.
4 K. Shankar, G.K. Mor, H.E. Prakasam, S. Yoriya, M. Paulose, O.K. Varghese and O.K. Grimes, *Nanotechnology*, 2007, **18**, 065707.
5 G.K. Mor, K. Shankar, M. Paulose, H.E. Prakasam, O.K. Varghese and O.K. Grimes, *Nano. Lett.*, 2006, **6**, 215-218.
6 J.A. Byrne, B.R. Eggins, N.M.D. Brown, B. McKinney and M. Rouse, *Appl. Catal. B: Environ.*, 1998, **17**, 25-36.

7 L. Ghimici and M. Nichifor, *Carbohyd. Polym.*, 2013, **98**, 1637-1643.
8 T. Mahmood, C. Cao, R. Ahmed, M. Ahmed, M.A. Saeed, A.A. Zafar, T. Husain and M.A. Kamran, *Sains Malays.*, 2013, **42**, 231-237.
9 J.Q. Liu, L.L. Ruan, S.B. Adeloju and Y.C. Wu. *Dalton Trans.*, 2014, **43**, 1706-1715.
10 C.J. Cai, M.W. Xu, S.J. Bao, C.C. Ji, Z.J. Lu and D.Z. Jia, *Nanotechnology*, 2013, **24**, 275602
11 G.Q. Lu and J.T.Y. Jr, *Chem. Rev.*, 1995, **95**, 735-758.
12 Y.Y. Wen and H.M. Ding, *Chin. J. Catal.*, 2011, **32**, 36-45.
13 Y.Q. Liang, Z.D. Cui, S.L. Zhu, Y. Liu and X.J. Yang, *J. Catal.*, 2011, **278**, 276-287.
14 L. Zhu, T. Ghosh, C.Y. Park, Z.D. Meng and W.C. Oh, *Chin. J. Catal.*, 20, **33**, 76-83.
15 S.S. Qian, C.S. Wang, W.J. Liu, Y.H. Zhu, W.J. Yao and X.H. Lu, *J. Mater. Chem.*, 2011, **21**, 4945-4952.
16 C.S. Lim, M.L. Chen and W.C. Oh, *Bull. Korean Chem. Soc.*, 2011, **32**, 1657-1661.
17 M. Wang, J.G. Jiang, J.W. Shi and L.J. Guo, *Appl. Mater. Interfaces*, 2013, **5**, 4021-4025.
18 Y.G. Zhang, L.L. Ma, J.L. Li and Y. Yu, *Environ. Sci. Technol.*, 2007, **41**, 6264-6269.
19 S.G. Yang, X. Quan, X.Y. Li, Y.Z. Liu, S. Chen and G.H. Chen, *Phys. Chem. Chem. Phys.*, 2004, **6**, 659-654.
20 M.K. Lee and T.H. Shih, *J. Electrochem. Soc.*, 2007, **154**, 49-51.
21 C.L. Yu, W.Q. Zhou, J.M. Yu, F.F. Cao and X. Li, *Chin. J. Chem.*, 2012, **30**, 721 -726.
22 D.Q. Zhang, M.C. Wen, B. Jiang, G.C. Li and J.C. Yu, *J. Hazard Mater.*, 2006, **211-212,** 104-111.
23 G.F. Liu, Fan. Qin, H. Yang, Z. Lu, H.Z. Sun, R. Chen, *Eur. J. Inorg. Chem.*,2012, **15**, 2508-2513.
24 W.L. Huang and Q.S. Zhu, *Comp. Mater. Sci.*, 2008, **43**, 1101-1108.
25 W.L. Huang, *Comp. Mater. Sci.*, 2012, **55**, 166-170.
26 W.L. Huang and Q.S. Zhu, *Comp. Mater. Sci.*, 2009, **46**, 1076-1084.
27 M. Shang, W.Z. Wang and L. Zhang, *J. Hazard Mater.*, 2009, **167**, 803-809.
28 Z.S. Liu, B.T. Wu, D.H. Xiang and Y.B. Zhu, *Mater. Res. Bull.*, 20, **47**, 3753-3757.
29 H.F. Cheng, B.B. Huang, P. Wang, Z.Y. Wang, Z.Z. Lou, J.P. Wang, X.Y. Qin, X.Y. Zhang and Y. Dai, *Chem. Commun.*, 2011, **47**, 7054-7056.
30 H.Q. Liu, X.N. Gu, F. Chen, J.L. Zhang, *Chinese J. Catal.*, 2011, **32**, 129-134.
31 W.Q. Fan, X. Q. Yu, S.Y. Song, H.Y. Bai, C. Zhang, D. Yan, C.B. Liu, Q. Wang and W.D. Shi, *CrystEngComm.*, 2014, **16**, 820-825.
32 Z.S. Liu, B.T. Wu, Y.B. Zhu, D.G. Yin and L.G. Wang, *Catal. Lett.*, 2012, **142**, 1489-1497.
33 Y.Y. Li, J.S. Wang, B.L. Liu, L.Y. Dang and Z.J. Li, *Chem. Phys. Lett.*, 2011, **508**, 102-106.
34 X. Zhang, L.Z. Zhang and D.J. Wang, *J. Phys. Chem. C*, 2009, **113**, 7371-7378.
35 K. Lalitha, G. Sadanandam, V.D. Kumari, M. Subrahmanyam, B. Sreedhar and N.Y. Hebalkar, *J. Phys. Chem. C*, 2010, **114**, 22181-22189.
36 D.F. Hou, X. L. Hu, Y.W. Wen, B. Shan, P. Hu, X.Q. Xiong, Y. Xiao and Y.H. Huang, *Phys. Chem. Chem. Phys.*, 2013, **15**, 20698-20705.
37 S.Y. Song, W. Gao, X. Wang, X.Y. Li, D.Y. Liu, Y. Xing and H.J. Zhang, *Dalton Trans.*, 2012, **41**,10472-10476.
38 J. Cao, B.Y. Xu, H.L. Lin, B.D. Luo, S.F. Chen, *Chem. Eng. J.*, 20, **185-186**, 91-99.
39 T.T.Y. Tan, C.K. Yip, D. Beydoun, R. Amal, *Chem. Eng. J.*, 2003, **95**, 179-186
40 X.X. Wei, H.T. Cui, S.Q. Guo, L.F. Zhao, W. Li, *J. Hazard Mater.*, 2013, **263**, 650-658.
41 J.G. Yu, W.G. Wang and B.Cheng, *Chem. Asian J.*, 2010, **5**, 2499-2506.
42 Y.L. Lee and Y.S. Lo, *Adv. Funct. Mater.*, 2009, **19**, 604.